ON ANALYSIS OF DUAL SPACECRAFT STEREOSCOPIC OBSERVATIONS TO DETERMINE THE THREE-DIMENSIONAL MORPHOLOGY AND PLASMA PROPERTIES OF SOLAR CORONAL FLUX TUBES

G. Allen Gary, John M. Davis, and Ronald Moore
Space Sciences Laboratory/ES82
NASA/Marshall Space Flight Center

Space Sciences Laboratory/ES82

George C. Marshall Space Flight Center/NASA

Huntsville, AL 35812, U.S.A.[1]

Received_____

Revised_____

---

[1] E-mail: Allen.Gary@msfc.nasa.gov

Abstract. By using two spacecraft equipped with multi-bandpass X-ray telescopes, it is possible to obtain direct 3-dimensional morphology of coronal structures which is essential for understanding the energetics and dynamics of the solar atmosphere. X-ray observations taken only in orbit about the Earth are inadequate to fully resolve the 3-dimensional nature of the solar corona. These Earth-orbit observations produce 2-dimensional images and an appropriate model must be included to derive the 3-dimensional structures from the line-of-sight information. Stereoscopic observations from space will remove this limitation and are needed if we are to improve our knowledge of the 3-dimensional morphology of the corona.

Several important points regarding a stereoscopic mission are investigated and illustrated using model coronal flux tubes and image-rendering techniques. Synthesized images are formed by integrating the emission from volume elements along the line-of-sight path through a 3-dimensional volume in which a set of model flux tubes are located. The flux tubes are defined by (1) a plasma model defining the emissivity for a specific density, temperature, and pressure distribution, and (2) a magnetic field model from which a set of field lines are selected to define the geometry of the flux tubes. The field lines are used to define the flux-tube volume by assuming an initial base radius and conservation of flux. An effective instrumental spectral-response function is folded into the integration. Analysis of pairs of these synthesized images with various angular perspectives are used to investigate the effect of angular separation on mission objectives. The resulting images and analysis provide guidelines for developing a stereoscopic mission.

Our study produced four important results, namely: (1) An angular separation of ~30 degrees maximizes the scientific return by direct triangulation analysis because of the tradeoff between increased line-of-sight resolution of position and decreased recognition of individual loop structures arising from the overlapping of multiple loops with increasing angular separation. (2) The analysis benefits from the use of time differential images to select flux tubes from the collection of numerous overlapping systems by selecting only recently heated or cooled flux tubes. (3) An analysis needs to be developed for algebraic reconstruction techniques applying a priori information, specific to the solar coronal structures, i.e., flux-tube continuity, maximum emission strength, non-negative emission, previous history, and maximum gradients of emission. (4) An

analysis strategy combining triangulation, modeling techniques, and algebraic restoration is necessary to derive a complete understanding of the 3-dimensional morphology of the magnetic field. In the same way that helioseismology is classical viewing of the Sun with a tailored set of analysis tools for probing the interior of the Sun, heliostereoscopy is classical viewing of the X-ray emitting corona and requires a tailored set of analysis tools to deduce the true 3-dimensional structure of the corona.

Subject Headings: Solar: Coronal Loops, Solar: Magnetic Fields, Telescope: Space Flight Instrumentation, Solar: Stereoscopic Missions

ON ANALYSIS OF   DUAL SPACECRAFT STEREOSCOPIC OBSERVATIONS TO DETERMINE THE THREE-DIMENSIONAL MORPHOLOGY AND PLASMA PROPERTIES OF SOLAR CORONAL FLUX TUBES

1. INTRODUCTION

1.1 THE IMPORTANCE OF HELIOSTEREOSCOPY

Heliostereoscopy uses multiple views of the X-ray emitting corona at different aspect angles and an appropriate set of analysis tools to provide a physical description of the true 3-dimensional structure of the corona which includes both the magnetic field and the distribution of the coronal plasma. The importance of the analysis tools in heliostereoscopy is similar to the importance of the analysis tools developed for helioseismology. In both cases the analysis tools tap the potential of the corresponding observations to explore a new aspect of the Sun.   In this paper, heliostereoscopy and its analysis tools are demonstrated using the synthesized imaging tools developed by Gary (1996, 1997) and Alexander, Gary, and Thompson (1998) to give examples of the analysis procedures.

The concept of heliostereoscopy is not new, yet it is still one awaiting proper implementation. Batchelor (1994) published a set of pseudo 3-dimensional images of the solar corona using solar rotation parallax to perform stereoscopic analysis. With similar techniques, others have also investigated ground-based pseudo heliostereoscopy using radio observations. However, the only direct way to provide stereoscopic images is by separate interplanetary spacecraft, with one possibly being in a near-Earth orbit. An introduction to subject has been given by Davila (1994) and Schmidt and Bothmer (1996). Davila points out how multi-spacecraft images can be used to determine 3-dimensional structures of coronal features, e.g. active region magnetic fields, coronal loops, helmet streamers, and coronal hole walls. This paper expands on Davila's work by creating synthesized three-dimensional coronal structures that can be viewed from different aspect angles simulating the views from different spacecraft.   We have placed particular emphasis on what can be learned from a minimum mission consisting of only two spacecraft. We have developed an analysis approach in which the separate tools, or techniques, can be used separately or together to

reach the final result -- a 3-dimensional description of the solar corona. We have tested the effectiveness of the tools by analyzing a set of synthesized images of a coronal active region and have reached four important conclusions. (1) In any realistically complex active region it is difficult to identify the same feature on images from different views especially as the angle between the views increases beyond a certain value. Because of this fact, we find that there is an angular separation which maximizes the scientific return by direct triangulation analysis. This optimum angle lies in the range of 20° to 40°. (2) Time differential images can be used to select a subset of flux tubes within an active region from the numerous, complex overlapping flux tubes by selecting only recently heated or cooled flux tubes. This singles out these structures for triangulation studies. Hence a high cadence is desired in order to have a minimum number of coronal features changing per image pair and to select the most features over a given period of time. (3) Since coronal structures are optically thin, emission tomography can be used to determine their internal structure. However, for high fidelity , the multiplicative algebraic reconstruction technique that we propose needs to be applied with known constraints specific to the solar coronal structures, i.e., flux-tube continuity, maximum emission strength, non-negative emission, previous history, and maximum gradients of emission perpendicular and parallel to the line of sight. (4) Only by combining triangulation, modeling techniques, and algebraic reconstruction is it possible to realize the full potential of stereo imaging to reveal the 3-dimensional morphology of the corona.

1.2 HISTORICAL PERSPECTIVE

The first global-scale fully 3-dimensional image reconstruction of the magnetic field was presented by Altschuler (1979). A low-resolution, full Sun coronal image was generated by his model which applied potential magnetic field theory to line-of-sight magnetograms as the lower boundary condition. This pioneering study created a picture of the corona --- which is seen as a "confused collection of overlapping structures, with arches and rays" controlled by the magnetic field. This pioneering study's main result was the presentation of the large-scale 3-dimensional, coronal field. All the recent modeling studies all start from the basic premise of the importance of the magnetic field to defining coronal magnetic features (McClymont, Jiao, and Mikic 1997). The first attempts at heliostereoscopy used solar rotation to provide the multiple aspect angles for long-

lived structures. Benton and Sakurai (1985) applied triangulation methods based on solar-rotation of features observed Skylab XUV images to analyze large-scale, inter-region loops to determine the morphology of the magnetic field lines. They developed methods for centering the images and the matrix algebra required to apply triangulation methods to solar observations. The analysis was limited to a few loops and did not show any nonpotential results outside the error bounds. Although their analysis uses a set of spherical coordinate transformations the basic stereoscopic solution involves only simple trigonometry as used in surveying.

More complex analyses have been attempted by Hurlburt et al. (1994) who studied polar coronal plumes observed by Yohkoh/SXT against the dark sky background. By using solar rotation to provide symmetrically spaced views over a range of viewing angles covering 180° they were able to apply standard tomographic methods. However, for these features the variation of brightness with time severely reduced the quality of the reconstruction.

Batchelor (1994) used the Skylab S054 X-ray Telescope images to produce pseudo-stereoscopic images via solar rotation. He claimed that many coronal structures not visible in an individual image were clearly visible when the images were viewed stereoscopically; however, it is difficult to support this conclusion from a visual inspection of his results. Recently Liewer and DeJong (1997) have used Yohkoh SXT images and LCD viewing eyewear to provide high quality stereoscopic viewing of the large-scale, stable coronal features, although it does considerable less well with smaller more dynamic regions. Rotational tomography has also been applied to solar radio astronomy observations. Aschwanden and Bastian (1994) developed the basic approach for restoring the 3-dimensional structures from VLA observations and showed the limitations resulting from source confusion, source motion, differential rotation, and time variability to which it is subject.

Considering true solar stereoscopy, Davila's paper (1994) addressed the problem of solar tomography and laid out several important discussions concerning multi-spacecraft observations of the solar corona. He introduced the algebraic reconstruction technique in which the set of algebraic equations relating the 3-dimensional volume-emission values and the 2-dimentional image-pixel values are iteratively solved in a least-squares sense. He described the errors introduced by spatial resolution, the convergence of the method and its dependence on the number of spacecraft and their angular separation, and the effect of detector noise.

Schmidt and Bothmer (1996) reported on a stereoscopic mission with the second spacecraft at the L5 (or L4) Lagrangian point, a point equidistant from the Earth and Sun and in the orbit of the Earth. The semi-stable orbit gives an angular separation of $60°\pm3°$. They point out that the main objective of such observations would be to study the morphology and dynamics of the coronal plasma structures and their extension into interplanetary space. They provide a set of mission requirements and a flight scenario.

1.2 2. Non-Solar Physics but Related Studies

Solar stereoscopy can benefit from the large collection of literature related to volume reconstruction from the analysis of images (projections) found in a number of different disciplines, e.g. mathematical, medical, geological, and material sciences. The techniques include both radiological imaging and computerized tomography (e.g. Gordon and Herman 1974; Herman 1980; Barrett and Swindell 1981; Kak and Slaney 1988). The analysis tools are divided into transform methods or discrete reconstruction methods. The use of transform methods requires many views, i.e. many spacecraft which is not financially viable at the present, and therefore we are restricted to the discrete reconstruction techniques (Censor 1983). The iterative approach discussed in the sections below is derived from this literature and, specifically, from the approach that has been applied to auroral investigations.

There have been several effective efforts to implement tomographic inversion techniques in auroral research by Gustavsson (1992, 1997) for the Auroral Large Imaging System (ALIS) and by Frey et al. (1996 a,b) for the Max-Plank-Institute for Extraterrestrial Physics. The ALIS is a grid of 14 optical stations with a ~50 km baseline. An important result of this study was the successful application of the "Fast Maximum Likelihood with A Priori Entropy" (FMAPE) method which takes advantage of all previous measurements. Frey et al. reported on the use of a *two-station analysis* of auroral arcs and, for a theoretical example with noise, their analysis gives a root-mean-square error of less than 5% for images and 15-20% for the volume. This is an important paper for establishing the possibilities of a two-spacecraft mission and includes a discussion of earlier auroral studies (Solomon, Hays, and Abreu 1984; Aso et al. 1990, Jones et al. 1991).

1.3. STEREOSCOPIC MISSION OBJECTIVES

We have identified several key objectives for a stereoscopic program designed specifically to study the magnetic field morphology, magnetic free energy, and heating of the solar corona and which our analysis technique is capable of addressing. They are the following:

i. Determine the morphology, strength and evolution of the magnetic field in 3-dimensions by determining the full 3-D structure of coronal flux tubes through analysis of co-temporal and time differential stereo images (subtracted images).

ii. Determine the 3-dimensional structure of the temperature and density distributions as well as the magnetic field through multi-spectral analysis.

iii. Explore the extent to which field is non-force free by comparing the derived magnetic field morphology with force-free field extrapolations.

iv. Determine the 3-D morphology of the dynamic magnetic field in flares and coronal mass ejections, specifically, determine whether and where reconnection occurs in these events.

v. Determine definitively whether there are interacting loops by observing the enhanced emission from two perspectives. This will show whether the observed enhanced emission is due to increased heating/density or to line-of-sight effects. If there is a true interacting enhancement, the observations then define the position and volume of the corona that is receiving the enhanced heating.

vi. Determine the photospheric foot prints of coronal loops by downward extrapolation of the field lines. This allows an analysis of the importance of the photospheric velocity and the magnetic field in the heating of coronal loops.

1.4 MISSION SCENARIO

The minimum mission consists of two spacecraft, one of which we assume will be an existing instrument in Earth's orbit e.g. the NOAA GOES/SXI or the Yohkoh SXT, or at the L1 point

(SOHO/EIT). For the second, interplanetary, spacecraft orbits can be chosen that either lead or lag the Earth and arguments supporting either choice can be made. The primary advantage of lagging orbits is that they provide a preview of solar activity that is about to rotate onto the visible disk. In contrast leading orbits provide a better view of features in the Sun's western hemisphere which have better magnetic connectivity to the terrestrial system because of their location at the base of the solar wind generated Archimedian spiral that passes near the Earth. Technological considerations favor leading orbits since these fall inside the orbit of the Earth which reduces the requirement on the size of the solar arrays for a given power output and has maximum spatial resolution. For a minimum cost mission we suggest a Hohmann elliptical orbit in the Earth's orbital plane which gives a trajectory that minimizes the velocity relative to both the Earth and the Sun (Battin 1964). The details of the orbit are given in Appendix A as we shall see later, a 30° angular separation is optimum for triangulation studies and the chosen orbit (Figure 1) gives relatively long stay times at both 30° and 60° separations during a 2 year mission; these are retrograde regions in the orbit as viewed in the geocentric frame of reference. The spacecraft orbit has a perihelion distance about half way (0.4) to the orbit of Venus and also provides a secondary advantage of arriving at the L_4 Lagrangian point, 60° ahead of Earth at 1 AU. This provides a semi-stationary point if the additional propellant can be carried to recircularize the orbit there. The advantages of the L_5 point have been discussed by Schmidt and Bothmer (1996), but this would require an outward-bound Hohmann orbit and the images would have less resolution.

2. HELIOSTEREOSCOPY ANALYSIS STRATEGY

Once a sequence of simultaneous stereo images have been acquired the next question is how should they be analyzed. To this end, we have developed a hierarchy of analysis tools which include triangulation, modeling and tomographic analysis, of increasing complexity whose ultimate goal is to provide a fully 3-dimensional description of the distribution of coronal material and magnetic fields. Triangulation provides a first step for a survey of identifiable coronal emission features; synthesized image rendering of coronal models provides a forward analysis approach; and emission tomography provides a deconvolution of the solar corona. These

techniques are used in concert with photospheric magnetic field measurements and extrapolation techniques to provide the magnetic framework and multi-spectral imaging to provide plasma diagnostics.

2.1 TRIANGULATION AND STEREOSCOPIC ANALYSIS

Benton and Sakurai (1985) used triangulation methods on solar-rotated features of Skylab XUV images to analyze large-scale, inter-region loops to determine the morphology of the field lines. They discussed the basic triangulation techniques which have been reviewed more recently by Liewer et al. (1997). Their technique is based on the change in perspective resulting from solar rotation and works quite well for long lived, stable structures, e.g. coronal hole boundaries, but hardly at all for temporally varying features like active regions which are of course the most interesting.

With pairs of images recorded *at the same time from* different aspect angles, true stereoscopic analysis is straight forward and does not depend on having stable structures. In fact, the analysis can provide crucial 3-dimensional measurements of dynamical phenomena. However, it does depend on the ability to identify the same feature in both images which as we shall show later is neither easy nor straight forward. If we simply consider two images of a loop system above a planar surface viewed from angles θ and θ' measured from the zenith, then the two images, with image coordinates (ξ, ψ) and (ξ', ψ'), provide the heliocentric xyz-coordinate information for a recognizable point source (in each image) from the matrix equation:

$$
\begin{bmatrix}
1 & 0 & \sin\theta/\cos\theta \\
0 & 1 & 0 \\
\cos\theta'/\sin\theta' & 0 & 1
\end{bmatrix}
\begin{bmatrix}
x \\
y \\
z
\end{bmatrix}
=
\begin{bmatrix}
\xi/\cos\theta \\
1/2\ (\psi+\psi') \\
\xi'/\sin\theta'
\end{bmatrix}
\tag{1}
$$

where the x-axis lies parallel to the orbital plane and in the solar surface, the z-axis is perpendicular to the solar surface, and the y-axis is defined by a right-handed system (Figure 2) The image coordinate ξ– and ψ-axes are parallel with the surface coordinates x and y. The orthographic image coordinates assume both X-ray telescopes have the same plate scale. The

derived y position is then the average of the two image ψ-coordinates seen from the matrix equation above for y; if the observations are perfectly aligned, $\psi=\psi'$. For $\theta=0$ the image is taken from directly above and cannot provide any information about the z-coordinate; the z-coordinate information is given only by the second image.

In order to demonstrate the results of the application of these techniques to solar images, we have developed a set of computer generated images based on the loop rendering technique of Gary (1997). This technique generates a set of 2-dimensional synthesized images by rendering the 3-dimensional magnetic field into coronal loops. A set of field lines are selected, and by employing appropriate coronal assumptions, the emission from the coronal flux tubes are rendered into images for a given aspect angle. Varying the assumptions on the emissivity values for the flux tubes, e.g., the density function, an algorithm has been developed to converge the synthesized images to the observed images, in this case Yohkoh SXT images. The result is a 3-dimensional model of the corona consistent with single view-point images. Figure 3 shows a series of synthesized images of the model coronal loop system as seen from various angles. The images were generated by rotating the volume containing the set of optically-thin coronal loops about an axis perpendicular to the line of sight. From inspection of Figure 3, it is clear that it is never easy to recognize the same feature in different images and it becomes increasingly more difficult as the separation angle increases and as the individual loops become nested in an overlapping complex with only the largest trans-equatorial loops being easily identifiable as the same loops seen at CMP.

In Figure 4, we represent this inability to distinguish loops as an accumulation error function which is modeled by a $\sin \theta$ function . The $\sin \theta$-function is selected on the assumption that the difficulty of recognizing individual loops is related to the ratio of a unit surface area to its projection at an angle θ. It is seen that beyond $40°$ the error in identification of the individual flux tubes becomes acute. On the other hand, the position error from triangulation becomes increasingly smaller with increasing separation. Hence, an angular separation between $20°$ and $40°$, by compromising between the triangulation analysis and the ability to identify features maximizes the scientific return. It can be shown that the position error for height is given by $[\Delta x^2 \cos^2 \theta' + \Delta x'^2] / \sin \theta'$ for the case $\theta=0$ where Δx and $\Delta x'$ are the linear spatial resolutions at the

Sun of the respective spacecraft. The position error function in units of Δx (=$\Delta x'$) is shown in Figure 4. It is seen that as the separation angle increases the position error decreases, which would imply having a second spacecraft with the largest possible angular separation. However, this conclusion has to be tempered by the difficulty of recognizing specific points in both stereoscopic images which correspond to the same point in the three-dimensional space as described earlier.

Using the pair of synthesized images for which θ and θ' are at $0°$ and $30°$ respectively, we have developed an IDL program to test the implementation of the matrix equation (Eqn.1). A field line is traced out, using a cursor to generate a set of points on the two images at the same y-value (shown as horizontal lines); a curve fit routine uses the set of points to produce a smooth 3-dimensional function for the coronal flux tube. An example is shown in Figure 5. In the example the projected origins of the two imagers coincide at the xyz-origin on the solar surface while the coronal points intersect above the photosphere. (The planar assumption applies only to the coordinate system and not to the geometry of the object.) In general the problem of spherical, Sun-center coordinates requires only a slight modification to these triangulation equations. For a loop in the x-z plane (the orbital plane), without any specially enhanced points, Equation 1 cannot provide any height information. This is a restriction for any 2-spacecraft mission and additional information is required if we are to define the third coordinate for loops which lie in the orbital plane. Loops that make an angle with the orbital plane allow unique solutions to the trigonometric equations and hence provide coronal height information.

Where applicable the triangulation process maps coronal flux tubes in an xyz-coordinate system and provides a *complete 3-dimensional analysis*. The derived flux tube geometries can be compared with potential field lines, calculated from photospheric magnetic field measurement. A set of extrapolated field lines that have foot points on equally-spaced grid points with the resolution of the magnetogram can be generated. This set would span the volume, i.e. giving a field line(s) near each flux tube. A least-squares comparison between this set and the set of "field lines" derived by triangulation gives a sense of the non-potential nature of the magnetic field. In the same way any nonpotential magnetic filed model can be tested against the 3-D field lines derived by triangulation.

2.1.1 Difference Imaging

We have emphasized the   difficulty in co-registering the structures observed in stereo pairs. However, our studies have indicated several avenues which will assist this process.   The first makes use of the fact that the active corona is continuously undergoing transient brightenings. An excellent example of this variation of the corona is reported by Shimizu et al. (1992) for the active region NOAA 6991 (30 Oct 1991). From 18:14 to 23:57 UT numerous transient brightenings of various sizes are observed. Typically, for these brightenings the physical parameters from SXT are: length: $5x10^3$-$4x10^4$ km, duration: 2-7 min, temperature: 4-8 MK, pressure: 5-20 dyn cm^{-2} and total radiative energy loss $5x10^{26}$ -$5x10^{29}$ ergs (Shimizu 1995). For a range of energy loss of $5x10^{26}$ -$5x10^{29}$ ergs   (or for a higher energy range of $5x10^{27}$ - $5x10^{29}$ ergs) we obtain, by integration, 860 (or 250) brightening events per day, assuming Shimizu's frequency distribution of dN/dE ~ $10^{-26}E^{-1.5}$ per day. To simulate this type of activity, we generated a pair of stereoscopic images with each image formed by subtraction of two images from the same spacecraft but at different times. In generating the images we assumed that several loops have doubled their emission and the rest have a normal distribution of 10 percent about their original values. The resulting difference images are shown in Figure 6 where the left panel is for an aspect angle of 0° and the right panel is for an aspect angel of 30°. For these specific aspect angles, these views are obtained from differences of the images A (0°) and C (30°) of Figure 3 with the loop density varied as just described. It is clear that temporal subtraction is a powerful technique to remove the confusion generated by overlapping loops. We can easily identify three bright loop systems (A, B ,and C) here that are not seen in the corresponding view of Figure 3 because of the complexity resulting from the line-of-sight integration effects. Such difference will be used in the section on volume reconstruction. This technique allows a clear identification of specific loops from the overall complex of loops.

The ability to identify specific loops leads to an interesting possibility of being able to determine the structures in the centers of active regions where the confusion from overlapping loops is most

severe. The process consists of rendering first the outermost loops from footpoint to footpoint and then removing this signature from the reconstructed image. By working inward removing loops one at a time and removing any loops that were identified by the differencing technique it may prove possible to identify and follow all the loops in the ensemble as the active region evolves. Finally, where it is possible to identify loops with individual field lines it will also be possible to unambiguously identify the loop footpoints to the photosphere in order to explore the characteristics of these sites which are responsible for loop heating.

2.2 FORWARD RECONSTRUCTION BY MODELING

The next stage of the analysis combines rendering of synthesized flux loops with the stereo observations to further extract the 3-dimensional structure of the corona. In this context 3-dimensional structure implies not only a knowledge of the external shape of the features but also an estimate of the distribution of plasma temperature and density along the line of sight. The general modeling technique (Gary 1997) has been applied to single images to test models of the magnetic field and the physical characteristics of the plasma within the coronal loops. By having two views, the process is enhanced for it requires the model to agree with both views which strengthens the 3-dimensional validity of the model. It is important to note that the synthesized images of the rendering process are a *forward process* in that there is no matrix or integral to be inverted, there is only a direct comparison of the generated images with observations.

To start, a model of the coronal field is generated from observations of the photospheric magnetic field. In this study, we have used the potential field model of Sakurai (1982). From the set of computed field lines, individual field lines are selected and a plasma filled 3-dimensional flux tube structure generated using the physical model (scaling laws) of Rosner, Tucker and Vaiana (RTV)(1978). By integrating the plasma emission along the line of sight and employing an instrument spectral response function, a rendered image of a single flux tube is obtained. The subset of all the individual flux-tube images can be selected by a non-negative least squares technique which is iterated to provide the best match with an observed X-ray image. This scheme minimizes the squares of the differences between synthesized image of the subset and the observed image with a non-negative constraint on the coefficients of the brightness of the individual flux-tube loops. The best derived images are used to infer the specific photospheric foot

points and   physical data from the   specific model employed. This analysis is important in determining directly the magnetic field configuration, which provides the structure of coronal loops, and indirectly, by inferring the magnetic field photospheric origins of the electric currents or waves, which provide the energy for the heating of the plasma. Given a solution (i.e., a geometric and physical model) which fits the images from one perspective, the solution can be verified by generating an image for the second perspective view and checking for consistency and then iterating between the two. The process is enhanced if the imagery also provides temperature diagnostics which can be incorporated into the total modeling effort.

In order to show the effect of the instrumental spectral profile on a heliostereoscopy mission and to demonstrate the effectiveness of modeling the solar corona by rendering flux tubes, we present in Figure 7 the effect of the instrumental spectral response function on the image and the information contained. The transequatorial active regions AR 7645 and AR 7646/47 (1994 January 4) are used. Gary (1997) has given a complete discussion of the data set for the complex and the image synthesization process. In the upper left panel of Figure 7, the observed Yohkoh/SXT image is shown which can be compared with the synthesized image in the upper right panel. This provides a baseline for the rendering process when the spectral profiles of the filters are included in the integration process. This panel and the bottom two panels show synthesized images using the instrument spectral response function for Yohkoh/SXT (AlMg, ~4MK), SAO/NIXT(~1.5MK), and GOES/SXI(open, ~1MK) soft X-ray imagers. The flux tubes temperature distribution and the instrumental spectral response from these instruments are then folded into the line-of-sight paths in order to form these synthesized images. With increasing sensitivity to the lower temperature, the footpoint locations can be better inferred and their location improved via downward extrapolation (Alexander, Gary, and Thompson 1998). It is seen that the image obtained in the open filter position of GOES/SXI is near to that obtain by the NIXT. This simulation shows that a pair of GOES/SXI-like instruments would be suitable for pioneering a minimum stereoscopic mission. The images of Figure 7 are generated using RTV analysis to obtain the density and temperature profiles along the arclength for a given pressure. For the derived emission measure and temperature, the results are convoluted with an instrument spectral response for the model corona.

The synthesized Yohkoh/SXT image and the actual SXT image are seen to be similar. The difference would be reduced by employing a more detail geometric and physical model. Having two separate images at different aspect angles would provide key information for improving the model.

In Figure 7, we have used the RTV analysis and the instrumental filter profiles convolved with a coronal model. In Section 2.4, we have used isothermal flux tubes and, hence, have removed any dependency on any specific instrumental spectral response function. This also has allowed a faster computation.

2.3 TOMOGRAPHY BY DISCRETE RECONSTRUCTION TECHNIQUES

Tomography is the general process of reconstructing a 3-dimensional volume by using a set of 2-dimensional images of the internal emission from different angles. The triangulation inversion and forward modeling techniques are mathematically unsophisticated attempts to derive the 3-dimensional distribution of the diffuse, optically-thin plasma of the solar corona without resorting to tomography. In our situation, where the number of views is extremely limited the normal tomographic inversion technique using Fourier analysis is inadequate and a special approach based on algebraic reconstruction techniques is necessary, all of which employ a least-squares iterative solution (Gordon and Herman 1974; Budinger and Gullberg 1977; Budinger, Gullberg, and Huesman 1979).

The first study of tomography for heliostereoscopy was performed by Davila (1994) for singular multiple spacecraft. For the limiting case of only two spacecraft, i.e., our minimum spacecraft mission, Davila's scheme produces unacceptable artifacts and has to be modified by use of additional constraints provided by ancillary data. All general discrete image-reconstruction techniques introduce a 3-dimensional Cartesian grid (e.g., NxNxN) covering the volume of interest, e.g. in our case an active region from the photosphere to some height in the corona. By assuming an initial distribution, a general iteration process gives an estimate for the emission values (plasma emissivity) for all these individual volume elements (voxels) by employing a mathematical algorithm using image-pixel values obtained by a set of stereo observations (see Appendix B). When the derived volume distribution is 'viewed', the resulting reconstructed

images must be the same, within the error bounds, as the observed images in order to have a solution. For coronal observations, the relatively small solar diameter and the large Sun-Earth distance (~1:100), allow us to approximate the viewing distance as infinite. Furthermore, one can consider the volume as consisting of a set of many single, plane-parallel planes, e.g. individual y=constant slices, (after Davila 1994). In this analysis all the slices are parallel to the Earth-spacecraft orbital plane. We can now restrict the analysis discussion to only one of these individual slices in the region of interest, since the total volume is obtained by stacking these slices. We can represent a slice by a thin 2-D slab of voxels with individual emission f(i,j) (or in vector form $f(k) \equiv f_k$ with $k_{max}=N^2$), and the corresponding images are now a set of two rows of pixels formed from the pair of 2-dimensional observational images (see Kak and Slaney 1988 and Davila 1994) . The pixel values are the line-of-sight integrals along a ray with the cross section of a pixel and, for a specific orientation, the set of pixels are known as projections. The individual rows of pixels from each stereoscopic image p_1 and p_2 are combined into a single vector p of length (M=2N) equal to the width of the images (N) times the total number of stereoscopic observations (2). For the optically thin X-ray emission of the corona, the brightness of each image pixel is the line integral through the plasma. For a single slice, the discrete reconstruction problem can be written as follows: Given the set of image pixels p, the problem is to find an estimate of the emission distribution f over the voxels from the under-determined linear equation:

$$p = R \ f + \ e, \tag{2}$$

where R is the geometric projection matrix with elements r_{mk} corresponding to the geometric contribution of f_k of the volume emission to the image pixel $p(m) \equiv p_m$. The elements of R, r_{mk}, are determined by the geometric contribution of the voxel k to the line-of-sight integral of path m, i.e., the intersection of the ray column with the voxel. (For normal or perpendicular views of the grid, each ray intersects a row or column exactly, and the r_{mk}'s are either 0 or 1.) The observational noise vector e represents the error. The solution of the discrete tomography problem (Eqn. 2) is an inverse problem; however the general direct matrix-inversion techniques are not appropriate and special iteration schemes have to be employed for a small set of images where there are more unknowns (f_k) than the number of constraining equations (Barrett and Swindel 1981, p. 434).

2.3.1 The Frey Approach: Modified Multiplicative Algebraic Reconstruction Technique

With only two spacecraft the algebraic reconstruction technique as presented by Davila (1994) cannot be used successfully for it produces too many artifacts. We have adopted a different approach first proposed and used by Frey et al. (1996a,b) to successfully reconstruct auroral structures from only two views. Their success was accomplished by introducing additional information to complement the lack of information available for the solution of Equation 2. The Frey method combines a multiplicative algebraic reconstruction technique (MART) with an initial guess derived from the back projection method (Appendix B). The MART uses the following iteration algorithm to solve for the emission distribution:

$$ f_j^{(i)} \quad = \quad f_j^{(i-1)} \quad \cdot \quad \left(\frac{p_m}{\sum\limits_k r_{mk} \, f_k^{(i-1)}} \right)^{\gamma} \quad , \quad \text{(cyclically through m)} \qquad (3) $$

where i refers to the current iteration and i-1 refers to the last iteration. The denominator is the reprojection defined by the line-of-path integrals $p_m' = \Sigma_k \; r_{mk} \, f_k$. This MART process updates the last iteration of the emission distribution by a set of ratios of the observed projection p_m to the reprojection raised to some power γ $(< 1$), where γ determines the speed of convergence (Censor 1983). The iteration continues until a specific criterion is satisfied. The initial distribution values are taken as the minimum of the unnormalized back projections for the various projections which are defined by

$$ f_j^{(0)} = \text{Min} \, [\Sigma_m \; r_{mk} \, p_m \,]. \qquad (4) $$

The resulting initial values are related to the average of all the image pixels associated with this voxel. The sum m is over the various geometric intersections and over all projections, the associated pixels $p_{m's}$, which contribute to the specific voxel associated with f_j. The back projection is used only to give a qualitative estimate, but not a good quantitative measure of the

volume emission (Llacer and Veklerov 1989a,b). However, it does give the limits of the region, because the back projection process defines the null-emission voxels and the MART process holds them at zero. At each iteration, the back-projection correction for each new iteration uses the image quotients p_μ / p_μ'. This means that the content of each voxel along a ray is multiplied by p_μ / p_μ' for a single projection, where all μ's belong to a single image. Generally, the iterative reconstruction technique of MART is applied as per Equation 3, until the least-squares criteria between the reconstructed images and the actual images is satisfied, i.e.,

$$\chi_i^2 = \sum_v \sum_m [\, p_m - \sum_k r_{mk} \, f_k^{(i)} \,]^2 \; < \; \chi^2_k \tag{6}$$

where χ^2_k is a defined value dependent on the image noise. The double sum is over all stereoscopic images and all appropriate projections for the entire volume, i.e., all the slabs. Frey et al.(1996a,b) modify this criteria and stop the iteration when the following criteria is satisfied.:

$$\lambda_{k+1} > \lambda_k, \quad \text{where} \quad \lambda_k = \Sigma_i \,|\chi_i\,| \; / \; \Sigma_m \, p_m. \tag{7}$$

This parameter provides the regularization constraint on the norm of f and takes into account all the previous iterations. They point out that the stopping parameter λ is only a comparison test of the output images with the observed images. It does not guarantee agreement between the 3-dimensional distribution of the output and the actual volume. However, the reconstruction parameter Λ, giving the real comparison between the derived voxels and the true voxel emission,

$$\Lambda = \Sigma_{\text{all slices}} \, \Sigma_k \,|\, f_k^{(i)} - f_k^{(\text{input})} \,| \; / \; \Sigma_{\text{all slices}} \, \Sigma_k \, f_k^{(\text{input})}, \tag{8}$$

was shown by Frey et al. (1996a, Figure 6 and 7) to be closely correlated with λ in his test cases.

2.3.2 A Priori Information- A critical Improvement

Of critical importance to the success of the Frey process is the employment of a priori information. The additional information is used by adding constraints which increase the number of equations by decreasing the physical volume of the reconstruction which allows the contribution of many of the N^2 voxels to be set to zero.   In this way, the number of equations is reduced and becomes more nearly equal to the number of unknowns. A set of constraints which

is straightforward and conceptually obvious to implement consists of: (1) the emission must be non-negative, i.e., the minimum emission value for a voxel is zero; (2) the maximum emission value from a voxel is determined by the maximum temperature and emission measure, and the maximum contribution is determined by imposing the instrumental spectral response function; (3) maximum expected gradients must be consistent with the instrumental spatial resolution and the expected physical gradients; and (4) no X-ray emission may come from below the transition region. The method used to reduce the emission volume is to use magnetic field extrapolations to limit the space from which the emission is coming, i.e., to set voxels to zero where the emission is known *not* to be present (cf. Katsulai and Arimizu 1985). Since we do not have an exact magnetic field extrapolation nor a priori knowledge of where the emission occurs, we impose an extensive envelope to cover the emission which is consistent with model for the stereoscopic pair of images, yet is confining enough to remove the artifacts. By applying these constraints the resulting artifacts caused by using only two views are greatly reduced. The process shows that a priori information is critical in a dual spacecraft mission and provides the success of such a mission in terms of being able to use discrete reconstruction techniques to perform tomography. Although we have not yet included all the above constraints in our analysis, we have shown that by only using the gross structure of the magnetic field, a tomographic analysis of the corona can be accomplished with a two spacecraft mission.

2.4 DEMONSTRATION OF TOMOGRAPHIC RECONSTRUCTION FROM TWO SYNTHESIZED STEREOSCOPIC IMAGES

In this section we will apply Frey's MART analysis technique to our synthesized active region images to demonstrate both its performance and the types of ancillary data that are needed to increase its effectiveness. Initially, we apply the process with no a priori information to the stereographic pair with view angles of $0°$ and $30°$. The analysis uses image arrays of 128 x 128 pixels and a reconstruction volume of 128^3 voxels. The result of the Frey method of MART is shown in Figure 8 where it is applied to the transequatorial complex. At the top are the two stereoscopic images employed in the analysis. These images are obtained by the viewing the

volume from a 0° aspect angle, i.e., straight down upon the cubic volume along the z-axis, and from a 30° aspect angle, i.e., 30° from the z-axis in the x-z plane. The non-zero emission in the volume was generated from a set 187 flux tubes based on potential field lines with a base radius of 1.4×10^3 km (0.75 pixel units) and a pressure of 1.0 dyn cm^{-1} for the isothermal plasma (e.g., T~2 MK). Below the stereoscopic pair in Figure 8 the orthographic projected images of the volume along the z ,x, and y are shown, i.e., these panels show the orthogonal views of the investigated volume along the z-axis, the x-axis, the y-axis. The top row of the three panels is the exact volume for the stereoscopic pairs based on the set of isothermal flux tubes. The second row show the effects of the back projection technique, generated by the IDL RECON3.PRO routine, for the 0°-30° stereoscopic pair. The effect of this rendering procedure is to zero all volume pixels that must be zero based on the zero intensity values of the images and then smoothes out the remaining pixel information over the non-zero volume elements. This volume rendering is used as the first iteration in Frey's method. The result, which is a minimum entropy solution is shown, in the bottom row. Frey's MART keeps the zero volume elements zero while trying to simplify the emission distribution required in the reconstruction of the original stereoscopic images. There has been no a priori constraints applied and hence the reconstruction is very primitive and no useful information is obtained about the distribution of the emitting plasma.

The next stage was to attempt to isolate some of the loops; in this case using the temporal differencing technique (Section 2.2.1). The top panel of Figure 9 shows three separate coronal loops with two of the loops being very close together. The stereoscopic pair has the same perspective angles of 0° and 30° degrees from the normal. The next row of panels shows the actual volume as seen along the z-axis, x-axis, and y-axis, respectively. The bottom rows show the back projection solution and the Frey (MART) solution after 5 iterations. The "north-south" loop configurations are recovered, but the two loops are no longer resolved. A relaxation parameter, γ, was employed to keep the oscillations down in the iterations scheme, i.e., [p(exact)/p(project)] $^\gamma$ with $\gamma = 0.1$. The least-squares difference between the actual and the reconstruction volume is at its minimum. The only constraint applied is that there is no emission from below the photosphere. The loops in the plane of the cameras have a large uncertainty in the z-axis (loss of height information) as expected. This lack of information in the equatorial plane produces the large artifact "streaking" (indicated by the arrowhead).

Finally, Figure 10 shows the Frey method applied to a subset of loops with magnetic field extrapolation being employed to constrain the solution space. Panel layout is as in Figure 8 and 9, except the middle row is the initial configuration as defined using a magnetic field model. The constraining volume is shown by the outer envelope of this row. The final solution reproduces all the features of the exact volume with negligible artifacts. This illustrates the importance of using a priori knowledge with a 2-spacecraft stereoscopic mission. It is noted here that the exact field lines are not needed in defining the constraining volume; only an approximation is needed and the tomographic process will proceed successfully, as shown.

3. CONCLUSION

3.1 OVERVIEW

We have described a heliostereoscopy program. The key elements of the program are outlined in Figure 11 which lays out the analysis as a linked sequence of increasing difficulty in which each step uses the output of the more direct methods which precedes it. The scientific objectives that are met at each step of the analysis are identified. The minimum stereoscopic mission which we have defined employs only a single interplanetary spacecraft, which achieves an orbit with an 11 months period and a return apogee 30° ahead of the Earth. In combination with an Earth-orbiting spacecraft carrying identical instrumentation it provides stereoscopic pairs of coronal images. To increase the information that can be extracted from the images they are combined with photospheric magnetograms, EUV, optical, and other coronal observations. The sequence of data-analysis steps outlined in Figure 11 makes use of all the information available and hence relaxes the need to have multi-interplanetary spacecraft. The methods are (i) coronal triangulation, (ii) synthesized image rendering, and (iii) tomography by discrete reconstruction techniques. Each interplays with the other methods. The triangulation method provides a straight forward approach for surveying of the 3-D coronal structures without the need to introduce any ancillary observations or assumptions. Where applicable, triangulation will provide the full 3-dimensional structure of coronal loops for the first time without the use of *ad hoc* assumptions. The synthesized image renderings provide a forward-modeling approach in which the use of derived

temperatures, physical scaling laws, and magnetic field data are used to form images which are directly compared with observations from the two different aspect angles. Since the scaling laws are approximations based on the interpretation of 2-dimensional observations it is highly likely that a satisfactory match will require improvement of the scaling law themselves in addition to quantitative adjustment of the physical parameters. Finally, a backward-modeling approach employs tomography by discrete reconstruction algorithms. In particular, the multiplicative algebraic reconstruction technique (MART), as employed by Frey et al. (1996a,b), is used with *a priori* knowledge of the photospheric magnetic field. The extrapolated field is used to restrict the solution space for the MART process and provides for convergence consistent with the photospheric magnetic fields. This greatly improves the accuracy of the tomographic reconstruction.

The specific goal of the stereoscopic data analysis is to provide a true 3-dimensional model of the coronal structure which includes the magnetic field geometry and the physical (plasma temperature, density and pressure) structure of coronal loops, helmet streamers, coronal hole walls, and coronal mass ejections without recourse to ad hoc assumptions. This model, or more precisely, the series of models developed from a sequence of pairs of images will provide a better 3-D picture of coronal evolution. In particular, they will show how the coronal magnetic fields and structures respond to changes in the photospheric magnetic field. This evolution will be related to (i) the coronal heating and dynamics, and (ii) the build up and dissipation of magnetic field energy. The magnetic field variation with height can be determined from the expansion factor of the flux tubes. Improvements and verification of force-free field models can proceed since the observed field line topology in 3-dimensions can be compared with theoretical models. Observed changes in the 3-D magnetic topology will show when and where reconnection occurs. Even if we do not actually observe reconnection in progress, it should be possible to describe the field configurations with sufficient accuracy to show that a smooth transition between the field configuration before and after the event is impossible and that reconnection must have occurred. Investigations of coronal heating will be improved by removing line-of-sight effects and from improved determinations of coronal loop footpoints. X-ray observations of coronal loops show important sites of energy conversion; hence, 3-dimensional details of the structure, foot points, and environment of these loops will provide key information on coronal heating at large.

Measurement of the full 3-D velocity of moving emission features will provide details of the magnetic field expansion during heating and eruptive events. The observed coronal magnetic field structures provide a method to derive the total field configuration and hence the full magnetic energy of active regions and the free energy associated with them, and changes in the energy (cf. McClymont, Jiao, and Mikic 1997). With such an array of full 3-dimensional views of the corona above active regions and of the changes which result in and from this activity, solar eruption prediction schemes will be vastly improved.

3.2 RECOMMENDATIONS

Four results from this study are: (1) a single interplanetary imager at an angular separation of ~30 degrees provides a reasonable, simple addition to an Earth-orbiting imager to provide stereoscopic analysis. It will be the pathfinder for future more ambitions stereoscopic missions. (2) Our sequential data analysis approach allows two spacecraft to determine much of the 3-dimensional coronal magnetic structure. (3) The use of time differential images can select flux tubes from the numerous overlapping flux tubes by selecting only recently heated or cooled flux tubes. (4) For full analysis we need to develop algebraic reconstruction techniques applying known constraints specific to the solar coronal structures, i.e., flux-tube continuity, maximum emission strength, non-negative emission, previous history, and maximum gradients of emission perpendicular and parallel to the line of sight. A combination of synthesized image renderings and discrete tomography, which uses the magnetic field to structure the bases functions of Eqn. 2, should be pursued. (5) A progressive, iterative sequence of analysis methods which combines triangulation, modeling techniques, and algebraic restoration is essential to derive a complete description of the 3-dimensional morphology of the magnetic field.

Having established the mission profile and the necessary data analysis tools, it is now appropriate to propose a single interplanetary spacecraft mission, along with an existing Earth orbiting imager, which will provide the coronal surveying and the mapping out the 3-dimensional

nature of the coronal structures for the first time. A stereoscopic mission will be an excellent mission for following up the success of the SoHO, Yohkoh, and Ulysses.

Appendix A. The Interplanetary Orbit

One must have a semi-major axis, a_H, of the spacecraft orbit sufficiently different from 1 AU in order to provide significant angular separation between the spacecraft and the Earth in order to perform solar stereoscopy. The value for the semi-major axis is derived and its consequences discussed in this appendix. To have the spacecraft imager observe the Sun without degradation of spatial resolution we choose its perihelion inside the Earth orbit; hence $a_H < 1$. To minimize the energy requirement of the mission we choose a Hohmann orbit. For a spacecraft leaving the Earth, the Hohmann orbit is cotangential to the Earth orbit r_e, and then r_e will be the spacecraft orbit's apogee distance; hence, from orbital mechanics, $a_H = r_e (1+e_H)^{-1}$ (see Figure 1) (Battin 1964). This provides the minimum energy requirements for a given spacecraft to reach a perihelion distance r_i. It is the only orbit that minimizes both the velocity relative to the Earth and the Sun. If the interplanetary satellite is launched when the Earth is at perihelion, then the semi-major axis of the Hohmann orbit is

$$a_H = r_e(1+ e_H)^{-1} = r_i (1- e_H)^{-1}   \quad (A.1)$$

where e_H is the eccentricity of the Hohmann orbit, r_e is spacecraft's apogee but also is the Earth's perigee distance, and r_i is the spacecraft perigee distance. The eccentricity of the spacecraft orbit is then

$$e_H = (r_e - r_i)/(r_e + r_i). \quad (A.2)$$

Hence, given only the satellite's perihelion distance for a Holmann orbit leaving from Earth, the semi-major axis is determine and the period of the orbit. The period is given by Kepler's third law,

$$T = a_H^{3/2} \text{ years} \quad (A.3)$$

for a_H measured in AUs. The spacecraft will orbit back to the Earth orbit in T years, i.e. from apogee to apogee. Assuming no orbital precessions and since T<1, then the satellite will be ahead of the Earth by a satellite-Sun-Earth angle D , where

$$D = 360° (1-T). \quad (A.4)$$

When the spacecraft returns to its aphelion distant of ~1 AU it will have its minimum velocity. Near the apogee the spacecraft will have its minimum relative motion with respect to Earth; in fact, it will be negative (see Figure 1). To make intensive measurements at specific angular separations it is then optimum to have the main observations occur when the spacecraft returns to apogee. This will happen after one orbital period. For a desired angular separation of D = 30° then

$$T = 1 - (D / 360°) = 0.92 \text{ years},$$

$$a_H = T^{2/3} = 0.94 \text{ AU}, \quad (A.5)$$

$$e_H = r_e / a_H - 1 = 0.06, \text{ and}$$

$$r_i = 0.89 \text{ AU}.$$

Appendix B. Discrete Tomographic Analysis

Back Projection: The simplest reconstruction method is the process of projecting the pixels from individual images back along the ray path and assign each voxel the sum of all such pixels which intersect it. For a thin 2D slab of emission voxels f (i,j), [or f_k in vector form] and for a set of "row"-images P_ξ with each at specific angular orientation θ_ξ; the back-projected reconstructed emission voxels f'$_{bp}$(k) is given by the sum of all projections ξ,

$$f'_{bp}(k) = \Sigma_\xi \ P_\xi(k), \qquad (B.1)$$

where the notation $P_\xi(k)$ means the pixel value associated with the voxel k= (i,j) for the projection ξ. (Here we have set the geometric intersection to be unity). Hence, f'$_{bp}$(k) is approximation to f(k), but f'$_{bp}$$^{(k)}$ is not normalized. The "corrected" back-projected voxels are given by

$$f_{bp}(k) = f'_{bp}(k) \ * \ [\underline{T}_{projection}/T_{sum}] \qquad (B.2)$$

where

$$T_{projection} = \Sigma_{all \ pixels} \ P_\xi \qquad (B.3)$$

is the sum of all pixels for a given image at one specific angular orientation θ_ξ, and

$$T_{sum} = \Sigma_k \ f'_{bp}(k) \qquad (B.4)$$

is the total emission from the entire slab, i.e. the unnormalized emission back-projected emission from all the voxels in the entire slab (Budinger and Gullberg 1974).

This reconstruction method is very simple, however, it cannot give the true emission distribution even for an infinite number of projections. For infinite resolution and projections the inverse Radon transform could provide the true distribution ; but for finite resolution and finite projections, iterative methods, must be applied (Radon, 1917).

Iterative Schemes: All general iterative methods to solve under-determined linear equation (Eqn. 3) start with an initial approximation for the distribution of the emission contributions f of the voxels and then iterates to a solution, given some method to update to the next iterative step.

The basic concept is that, for a specific pixel value $p(k) = p_k$, the discrete reconstruction problem gives a set of linear equations for each ray and the associated voxels f_k of the form:

$$r_{s1} \, f_1 + r_{s2} \, f_2 + \ldots + r_{sk} \, f_k = p_s \quad , 1 \le k \le N, \; 1 \le s \le M \quad (B.5)$$

and hence these represent a hyperplane in an NxM-dimensional space, where we have set the noise e=0, for simplicity. The crossing of all these hyperplanes, or the least-squares solution of the minimum intersection distance, represents the solution, i.e., the estimate of the actual 3-dimensional distribution. In the Kacrmarz technique (also called ART for algebraic reconstruction technique) the iterative steps are given by the successive projections of the last iteration upon the various hyperplanes in a cyclic manner until the iterations are truncated (Rosenfeld and Kak 1982, Chong and Zak 1996). The iteration equation is given by

$$f_j^{(i)} = f_j^{(i-1)} - \frac{\left(\sum_k r_{mk} \cdot f_k^{(i-1)} - p_m \right)}{\left(\sum_k r_{mk} \right)^2} r_{mj} \quad , \text{(cyclically through m)} \quad (B.6)$$

where the k-sum refers to the voxel associated with only the ray for the pixel p_m and cycles completely through pixels m per iteration (i.e., both rows from the set of two images). (A good illustration of the geometric interpretation of this method is given by Kak and Slaney (1988, chapter 7)). Note that the ray sum $\sum_k r_{mk} f_k^{(i-1)}$ is the re-projection associated with the image pixel m at the (i-1)th iteration. This additive algebraic reconstruction technique (A-ART) is the approach employed by Davila (1994) and is strongly linked to the initial approximation for f_i.

An alternative to this unconstrained additive technique is the multiplicative analogy (MART) which explicitly insures only positive emission contributions and is an entropy minimization process, i.e. it yields a reconstruction with the lowest information content consistent with the stereoscopic images (Censor 1983, Bryne 1993). The iteration equation is given by:

$$f_j^{(i)} = f_j^{(i-1)} \cdot \left(\frac{p_m}{\sum_k r_{mk} f_k^{(i-1)}} \right)^{\gamma} \quad , \text{(cyclically through m)} \quad (B.7)$$

where if f_j is zero then it remains zero for all additional iterations. The relaxation parameter $0<\gamma\leq1$ can be introduced to improve the numerical convergence (Censor, 1983). The MART algorithm consists of taking an initial estimate of the voxels, $f_j^{(0)}$, and then modifying the voxel along each ray, m, by a factor that compensates for the discrepancy between the associated pixel value and the calculated pixel value for that ray, as given by the denominator. This is the method used with success by Frey et al. (1996a,b) with a pair of stereoscopic images of the aurora. In the standard MART algorithm termination at the ith iteration is reached when the parameter

$$\chi_i^2 = \sum_v \sum_m [\, p_m - \sum_k r_{mk}\ f_k^{(i)}\,]^2 \qquad\qquad (B.8)$$

is minimized for all slices v, e.g., a least-squares solution between the stereoscopic image pairs and the appropriate projections of the volume.

References

Aso, T., Hashimoto, T., Abe, M., Ono, T., and Ejiri, M.: 1990, J. Geomagn. Geoelectr. **42**, 579.

Alexander,D., Gary, G.A., and Thompson, B. J: 1998, Confer. Series ASP, Proc. 2nd Advances in Solar Physics Euroconference, Preveza, Greece.

Altschuler, M. D.: 1979, in Image Reconstruction from Projections: Implementation and Applications, ed. G. T. Herman, Academic Press, New York, p. 103.

Aschwanden, M. J., and Bastian, T. S.: 1994, *Astrophys. J.* **426**, 425.

Battin, R. H.: 1964, Astronautical Guidance, McGraw-Hill, New York, p. 100.

Barrett, H. H., and Swindell, W.: 1981, Radiological Imaging: The Theory of Image Formation, Detection, and Processing, Academic Press, New York.

Batchelor, D.: 1994, *Solar Phys.* **155**, 57.

Berton, R., and Sakurai, T.: 1985, *Solar Phys.* **96**, 93.

Budinger, T. F., and Gullberg, G. T.: 1977, *IEEE Trans. Nuclear. Sci.*, **NS-21**, 2.

Budinger, T. F., Gullberg, G. T., and Huesman, R. H.; 1979, in Image Reconstruction from

Projections: Implementation and Applications, ed. G. T. Herman, Academic Press, New York, p. 117.

Byrne, C. L.: 1993, *IEEE Trans. Image Proc.* **2**, 96.

Censor, Y.: 1983, *Proceed. IEEE* **71**, 409

Chong, E. K. P., and Zak, S. K.: 1996, An Introduction to Optimization, Wiley, New York, pp. 179 and 351.

Davila, J. E.: 1994, *Astrophys. J.* **423**, 871.

Frey, S, Frey, H. U., Carr, D. J., Bauer, O. H., and Haerendel, G.: 1996a, *J. Geoohys. Res.* **101**, 21731.

Frey, H. U., Frey, S., Bauer, O. H., and Haerendel, G.: 1996b, *SPIE* **2827**, 142.

Gary, G. A.: 1997, *Solar Phys.*, **174**, 241.

Gary, G. A.: 1996, SCOSTEP STEP WG-1, April 9-11, Huntsville, Al.

Golub, L., and Herant, M.: 1989, *SPIE* **1160**, 629.

Gordon, R., and Herman, G. T.:1974, *Int. Rev. of Cytology* **38**, 111.

Gustavsson, B.: 1992, A Study of Feasible Tomographic Inversion Techniques for ALIS, IRF Tech. Rpt. 039, Institutet for Rymdfysik, Kiruna, Sweden.

Gustavsson, B.: 1997, *J. Geophys. Res.*, in press.

Herman, G. T.: 1980, Image Reconstruction from Projections: The Fundamentals of Computerized Tomography, Academic Press, New York.

Hurlburt, N. E., Martens, P. C. H., Slater, G. L., and Jaffey, S. M.: 1994, in Solar Active Region Evolution: Comparing Models with Observations, ASP Conference Series 68, eds. K. S. Balasubramaniam and G. W. Simon, p. 30.

Jones, A. V., et al.: 1991, *Planet. Space Sci.* **39**, no. 12.

Kak, A. C., and Slaney, M.: 1988, Principles of Computerized Tomographic Imaging, IEEE Press, New York.

Katsulai, H. and Arimizu, N.: 1985, *IEEE Trans. Nuclear Sci.* **NS-32**, 1217

Liewer, P. C., and DeJong, E.: 1997, private communications

Liewer, P.C., Davis, J. M., DeJong, J. E., Klimchuk, J. A., Reinert, JR., Davila, J. M.: 1997, EOS, 78(17), S225.

Llacer, J., and Veklerov, E.: 1989, *IEEE Trans. Medical Imaging* **8**, 186.

Llacer, J., and Veklerov, E.: 1989, *Int. J. Imaging Systems and Tech.* **1**, 132.

McClymont, A. N., Jiao, L., and Mikic, Z.:1997, *Solar Phys.,* **174**, 191.

Pizzo, V.: 1997, private communication.

Puetter, R. C.: 1995, *Int. J. Image Systems Tech.,* in press.

Radon, J.: 1917, Ber. Saechs. Akad Wiss. Leipzig, Math Phys. **69**, 262

Rosenfeld, A., and Kak, A. C.: 1982, Digital Picture Processing, Vol 1., Academic Press, New York, Chapter 8.

Rosner, R., Tucker, W. H., and Vaiana, G. S.: 1978, *Astrophys. J.* **220**, 643.

Sakurai, T.: 1981, *Solar Phys.* **69**, 343.

Sakurai, T.: 1982, *Solar Phys.* **76**, 301.

Schmidt, W. K. H., and Bothmer, V.: *Adv. Space Res.* **17**, (4/5)369.

Shimizu, T., Tsuneta, S., Acton, L. W. , Lemen, J., and Uchida, Y.: 1992, *Publ. Astron Soc. Japan.* **44**, L147.

Solomon, S. C., Hays, P. B., and Abreu, V. J.: 1984, *Appl. Opt.* **23**, 3409.

Yohkoh Analysis Guide, 1993, Lockheed, Palo Alto, Ca.

Yoshida, T., and Ogama, Y.: 1995, *Publ. Astron. Soc. Japan* **47**, L15.

Figure Captions

Figure 1. The orbital analysis of a stereoscopic mission from both a heliocentric and geocentric viewpoint is shown. In the heliocentric view the Earth and the interplanetary spacecraft orbits the Sun as shown. The spacecraft orbit is inside the Earth's orbit but tangent to Earth's orbit at the Earth's perihelion. The spacecraft having a smaller semi-major axis returns to the Earth's orbit sooner than the Earth can revolve about the Sun. The spacecraft slowly moves ahead of the Earth even though the initial ejection velocity is opposite to the Earth velocity. Two relative locations of the Earth and the spacecraft are shown; H1 and H2, in the heliocenteric view and G1 and G2 in a geocentric view. Shown is the Earth orbit (solid circular line), the interplanetary spacecraft orbit (smaller circular solid line), a 1 AU reference circle (dashed), and the spacecraft orbit (thick line) from a geocentric viewpoint with a fixed Sun-Earth line (z-axis). The spacecraft moves ahead of the Earth and returns to a 1AU position 30° ahead of the Earth in 11 months and 60° in 22 months. The spacecraft is launched when the Earth is at perihelion distance. In the geocentric view the spacecraft makes a series of cyclic motions slowly moving further ahead of the Earth allowing stereoscopic observations with varying aspect angles. At the Sun a slice of the corona is shown which can be analyzed by a palette of techniques as discussed in the text.

Figure 2. The triangulation geometry for Equation 1 is shown.

Figure 3. Synthesized images of the model coronal loop system is shown at angles of $\theta = 0°$, 10°, 30°, 45°, 60°, and 90° from vertical (A, B, C, D, E, and F, respectively). A

stereoscopic pair can be made with the 0° image and any other image. We can consider the 0° image as being the image obtained from an Earth orbit X-ray imager and the other view as images obtained as the spacecraft moves out ahead of the Earth. When comparing the off-vertical views (B-C) with the vertical view (A), it becomes difficult to identify the same individual coronal loops as the aspect angle increases from 0°. Hence, the comparison of the images suggest that the 0°-30° stereoscopic pair is an optimum trade-off between separation and the ability to identify individual loops.

Figure 4. The position error function and accumulation error for the triangulation process is shown. The position error in height is given by $[\Delta x^2 \cos^2 \theta' + \Delta x'^{\,2}] / \sin \theta'$. The accumulation error, the inability to recognize the same loops in images with different aspect angles is estimated as a $\sin(\theta)$ function. Hence, the optimum angle of separation, taking into account both of these effects is about 30°.

Figure 5. A triangulation result is shown along with the 0°-30° stereoscopic pair and the magnetic field lines superimpose. The coronal loop which has been traced out in the stereoscopic pair is shown as a dark line over the bright loop. As points in the 0° image are traced out along a coronal flux tube a set of horizonal lines (constant y) are produced and protracted into the 30° image to be used for reference in tracing the same points in this image. After the triangulation analysis and for comparison, the actual field line associated with the derived field line was drawn. In the 3-dimensional view, the derived structure (solid line) using Equation 1 is shown along with the actual field line (dashed line).

Figure 6. The set of pseudo temporal images for the 0° and 30° aspect angles is shown. The images are derived by increasing the brightness of a set of loops by a factor of two and having the brightness randomly vary about 10% for the remaining loops and subtracting the two different pairs of images. This stereoscopic pair of temporal subtractive images illustrates a process to identify individual loops which would be lost in a complex of overlapping loops without applying the differentiation. Three such loops, A, B, and C, are marked in the left-hand panel (0° aspect angle).

Figure 7. Illustrated is the effect of the instrumental spectral profile on the resulting images. The

upper panels show a transequatorial complex as seen by the Yohkoh/SXT along with the synthesized image using the Yohkoh SXT instrumental spectral AlMg filter (Yohkoh Analysis Guide 1993). This set of images illustrates the ability to model the 3-dimensional corona using the rendering process discussed in the text. The upper right panel shows the synthesized image of the region employing the RTV hydrostatic equation with a *fixed* pressure of 1.0 dyn cm^{-2} and using potential field lines derived from a magnetogram. In the lower left panel is the synthesized image assuming the spectral response of the Harvard Smithsonian Center for Astrophysical/ Normal Incident X-Ray Telescope (CFA/NIXT) (Golub and Herant 1989, Yoshida et al. 1995). In the lower right is a synthesized GOES/SXI image using the open position configuration for the telescope (Pizzo 1997). The lower temperature response of the SXI image allows for a better determination of the foot-point locations associated with specific coronal loops as compared to the SXT response. Because the location of the foot points are important in relating the coronal loops to photospheric activity, the lower temperature sensitivity is desirable for the stereoscopic imagers.

Figure 8. The Frey's MART methods is applied to a multi-loop system of a transequatorial complex. The stereoscopic pair for the analysis is shown at the top. The z ,x, and y projection of a 128^3- volume of synthesized coronal loops using these 0° and 30° perspective views are shown below. The first panels of triplets show the orthogonal views of the investigated volume along the z-axis , the x-axis , the y-axis.   This row of projections is derived from the actual model used in forming the stereoscopic pair above. The second row of triplets is the back projection results generated by the IDL RECON3.PRO routine for the 0°-30° stereoscopic pair as discussed in the text. The Frey iteration result is shown in the bottom panel. Except for the assumption of no coronal emission from below the solar surface, there has been no a priori constraints applied and hence the reconstruction in very primitive.

Figure 9. The Frey's MART method is applied to a subset of loops which simulate a temporal subtractive process. The overall panel layout is as in Figure 8, i.e., the z ,x, and y projection of a 128^3-volume of synthesized coronal loops . The small set of loops represents loops selected by temporal subtraction techniques as illustrated in Figure 6. In

Frey's MART process the only constraint applied is that there is no emission from below the photosphere, as in Figure 8. The lack of information in the equatorial plane produces the large artifact (indicated by the circumflex). For simplicity, the background fluctuations of 10% for the other coronal loops of Figure 6 were set to zero.

Figure 10. The Frey's MART method is applied to the same subset of loops as Figure 9 with the addition constraint that a magnetic field extrapolation employed to constrain the solution space. Panel layout is as in Figure 8 except that the middle row is the initial configuration as defined using a magnetic field model. The large outer envelope shows the extended region employed as a priori limits for the reconstruction. A larger envelope simulates the lack of knowledge one would have in practice in knowing the exact field configuration. The inner envelop (white) is the actual coronal loop location as seen in these projections and allows one to see the amount the envelope has been enlarged. The envelope allows all the volume elements outside of the region to be set to zero and effectively increases the number of equations that we have for the emission distribution. The set of loops represents loops selected by temporal subtraction techniques as Figure 9. The envelope selection could be helped using the results for pure triangulation and comparing these results from various field extrapolations. The final solution for the Frey's MART reproduces all the features of the exact volume without any artifacts, and illustrates the importance of using a priori knowledge with a 2-spacecraft stereoscopic mission. An approximate solution is obtained via tomography using only two imagers.

Figure 11. The stereoscopic image analysis program for two spacecraft mission. The stereograms are analyzed first by triangulation to provide the 3-dimensional structure of the corona for those points which can be seen in both images. With the introduction of a magnetic field model the comparison of the linear features in the images with a set of associated field lines allows the determination of the appropriate magnetic field model. The physical characteristics of the plasma are included and synthesized images are rendered and compared with the stereoscopic images. A least-square comparison between the stereoscopic images and the render images employing various models provide additional information for the full tomographic analysis program using Frey's MART. A full 3-dimensional mode then results which are consistent with the X-ray observations. A

resulting time series of solutions provide a model for comparison with dynamical numerical models.

File=stereo_final Date: May 27, 1998/garyga

H1

SPACECRAFT ORBIT
(Geocentric View)

G2

G1

X

Z

SUN   SLAB

EARTH
(Geocentric View)

H2

SPACECRAFT ORBIT
(Heliocentric View)

1 AU

EARTH ORBIT
(Heliocentric View)

x - y image plane

x '- y ' image plane

Photosphere

Position Error Function / Accumulation Error Function vs. Stereographic Angular Separation
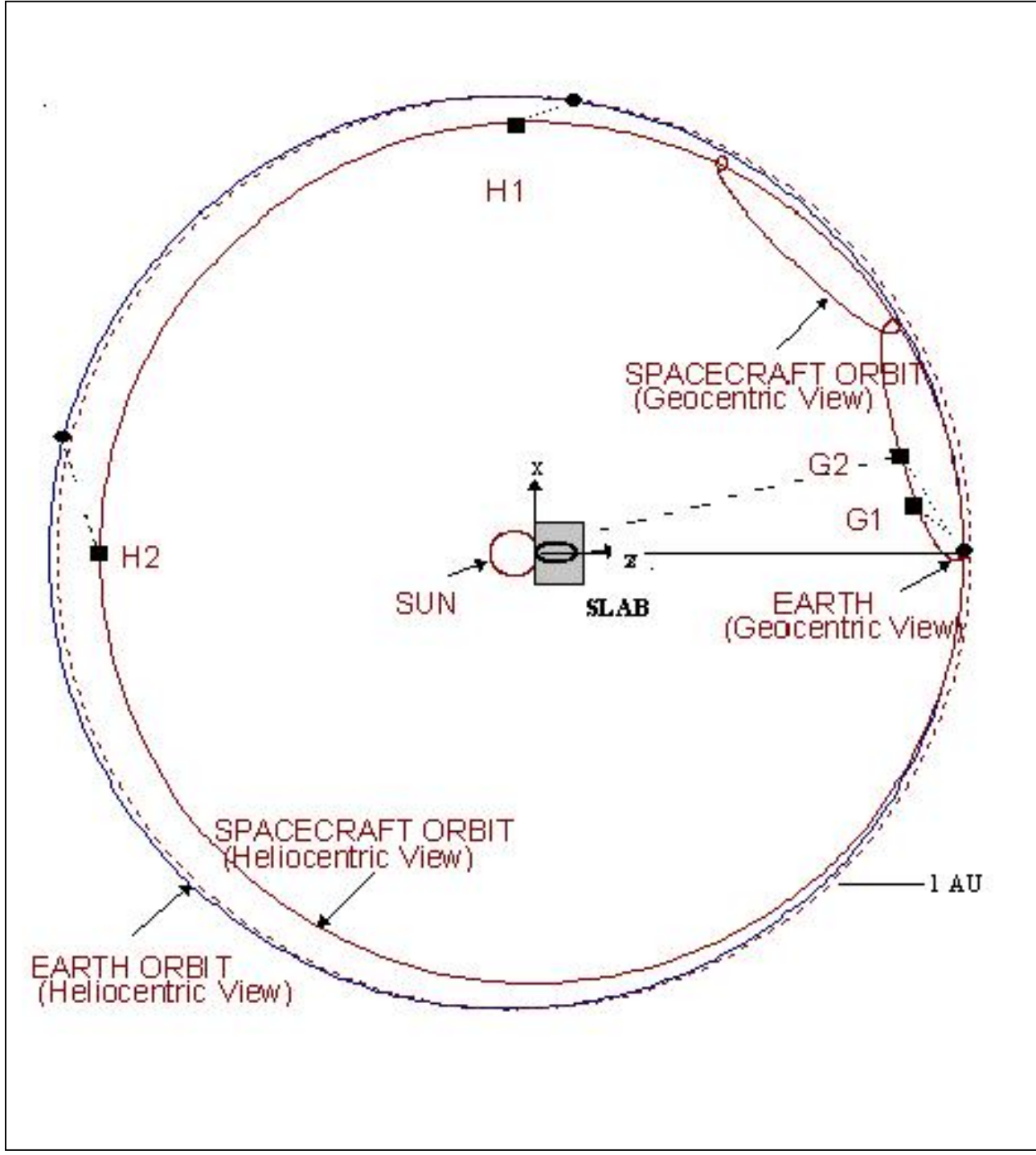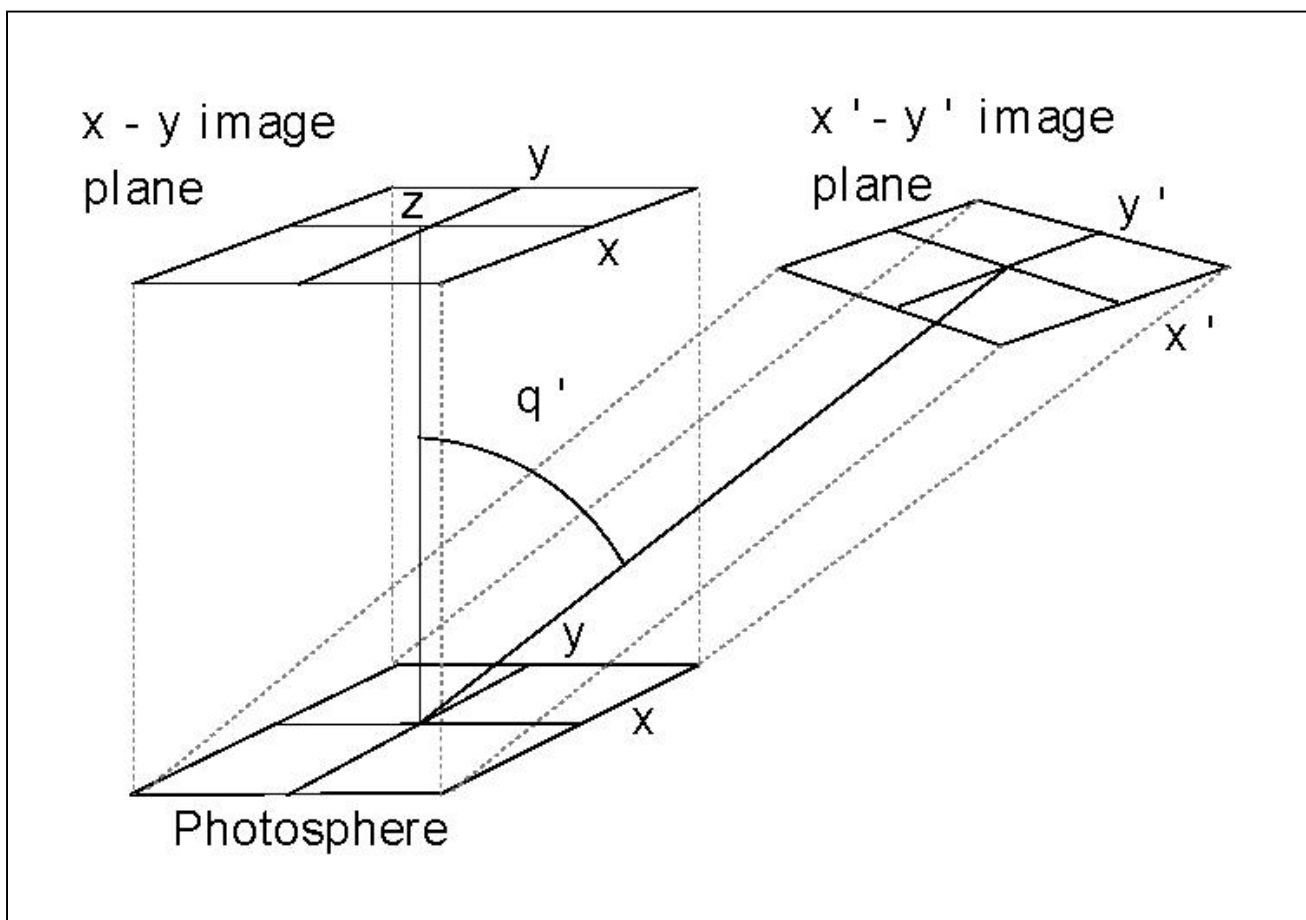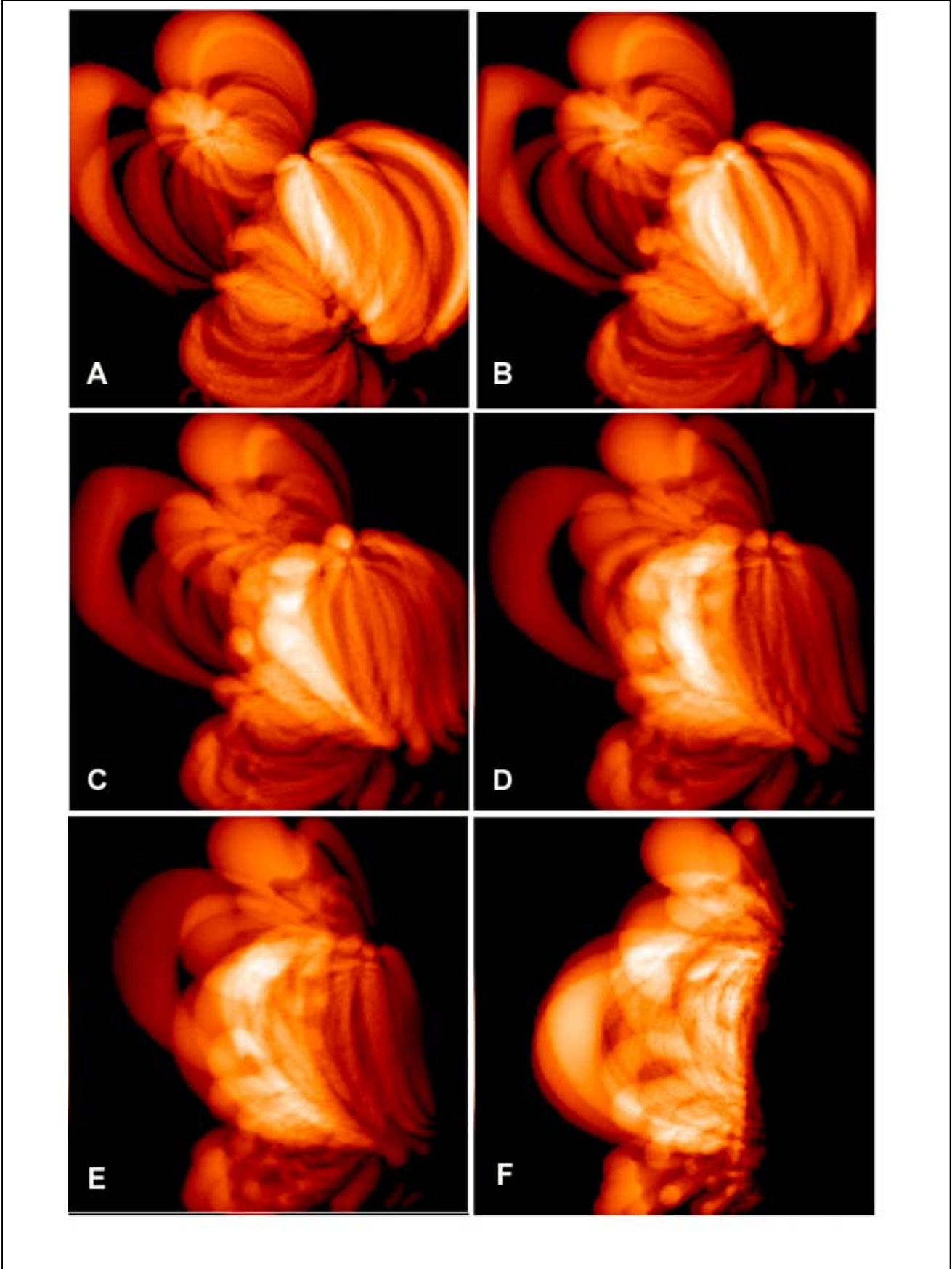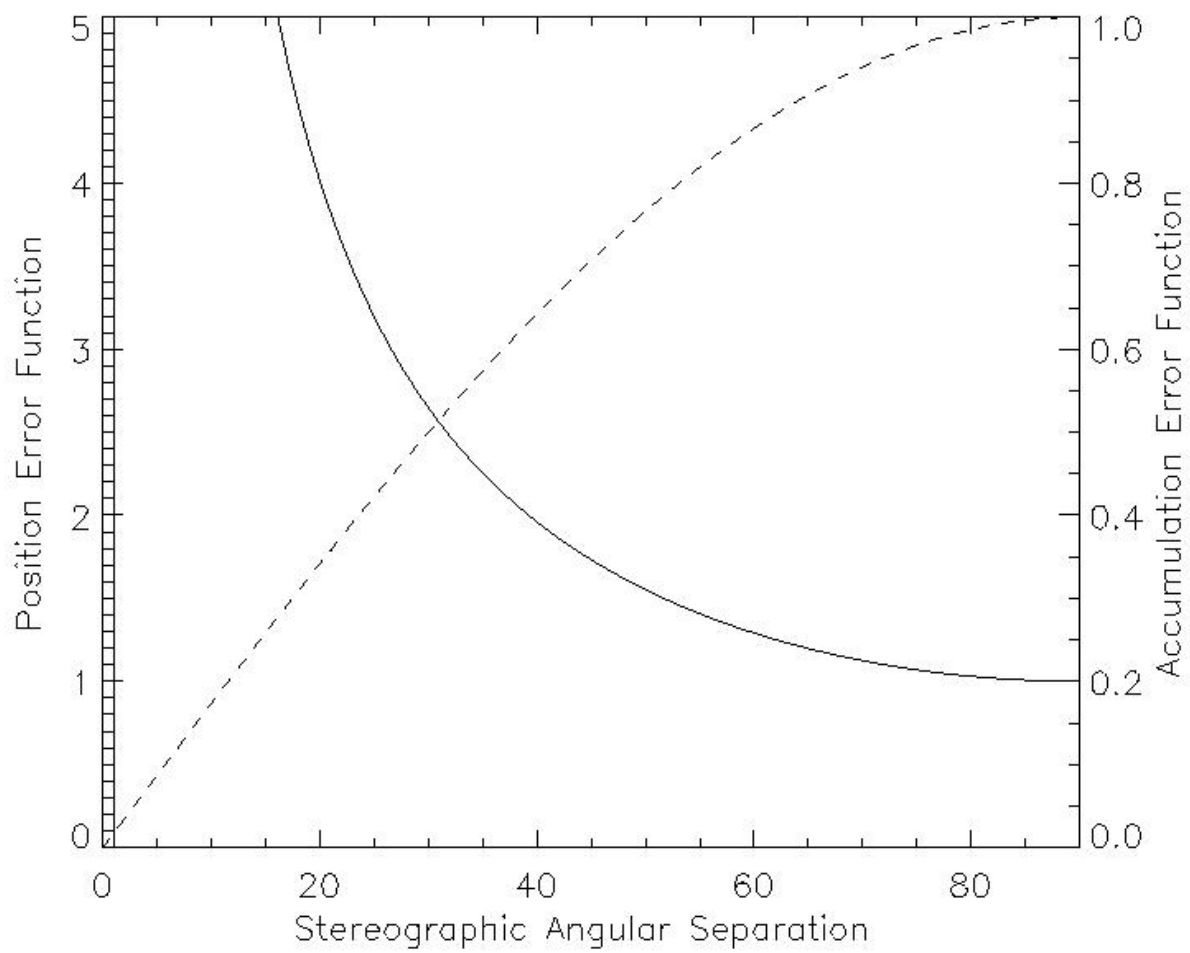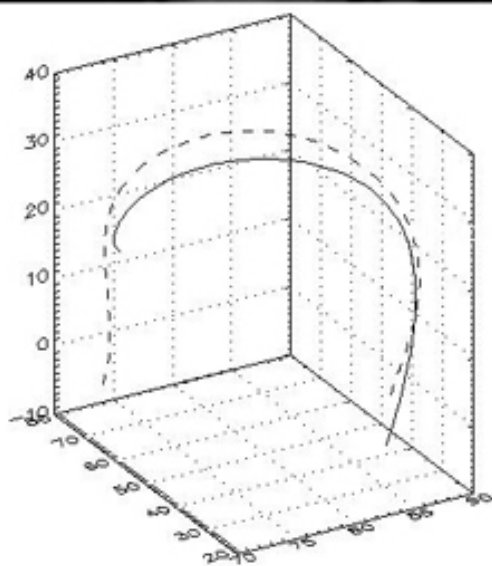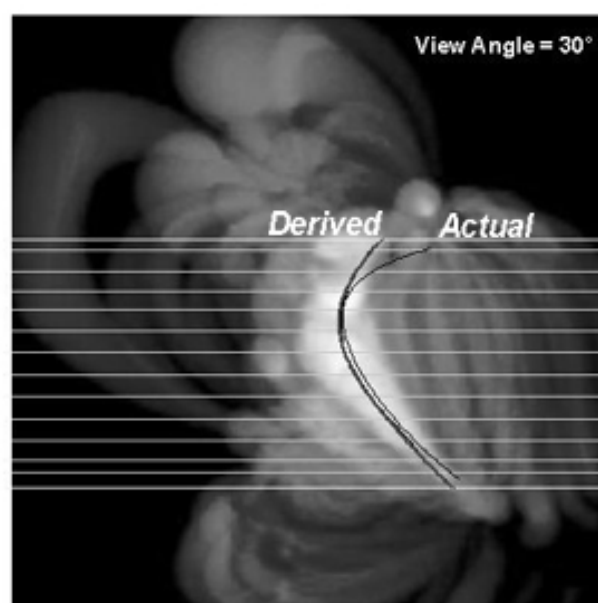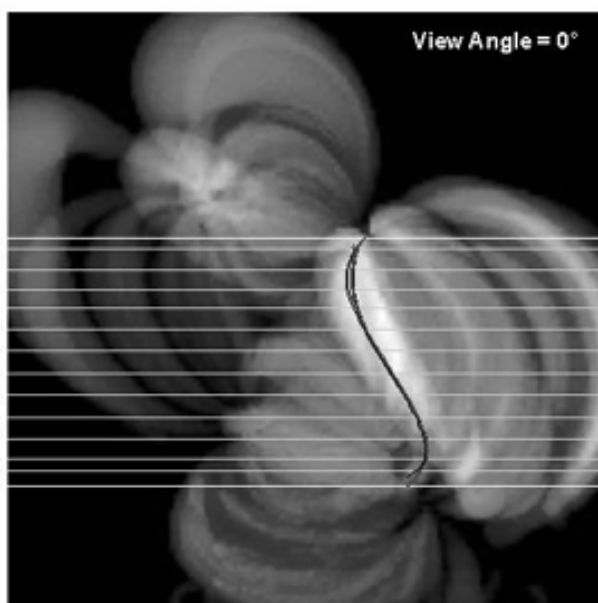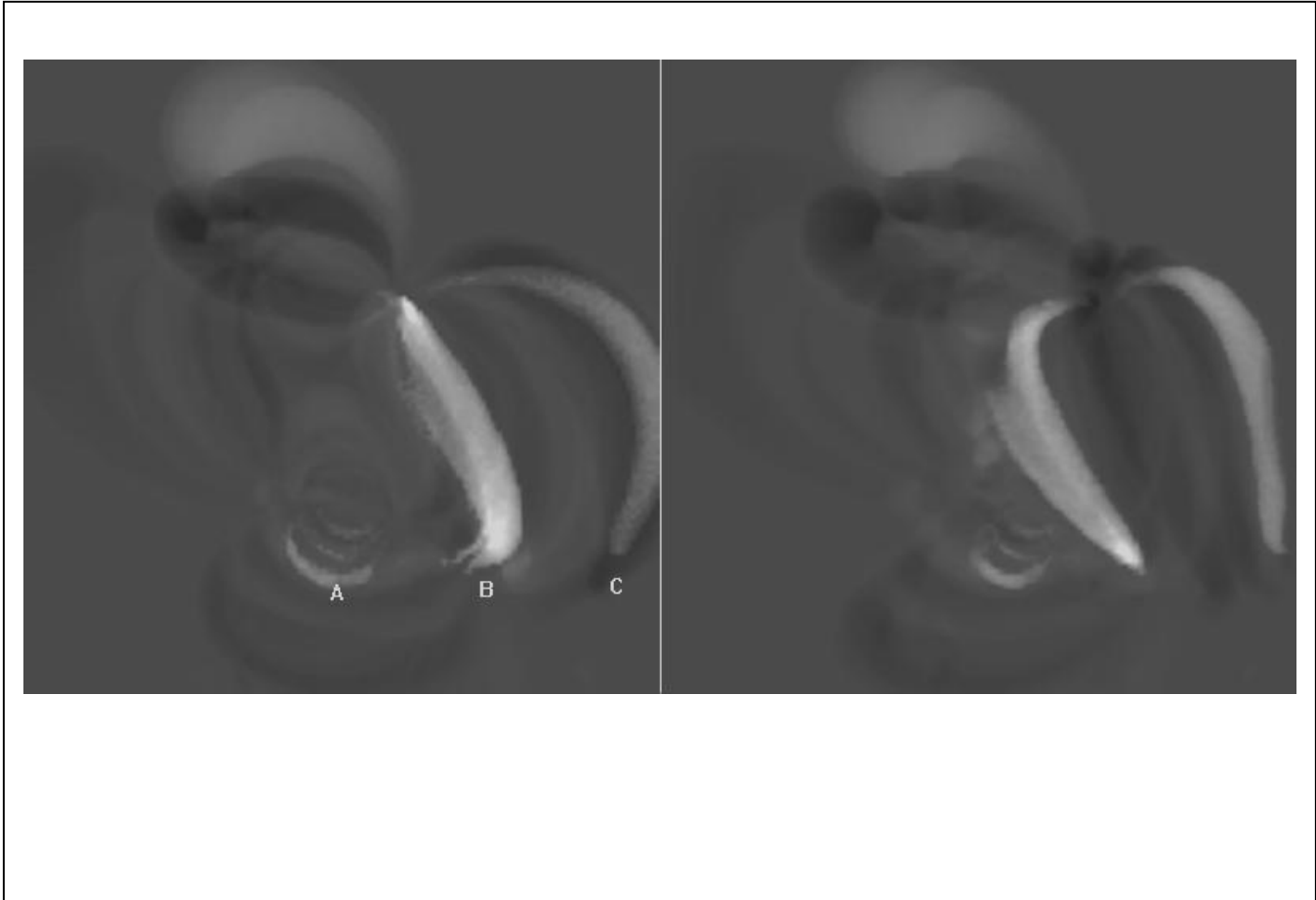
RENDERING SOLAR MAGNETIC FLUX TUBES

YOHKOH/SXT IMAGE

SYNTHESIZED SXT IMAGE

SYNTHESIZED NIXT IMAGE

SYNTHESIZED SXI IMAGE

Stereographic Pair

Z-projection X-projection Y-projection

Actual Volume

Back Projection

Frey MART Solution

Stereographic Pair

Z-projection   X-projection   Y-projection

Actual Volume

Constraining Volume

Frey MART Solution

*Scientific Objectives
Achieved at Each Step:*

*Analysis of geometric structures
in 3D of coronal loops, coronal walls,
helmet streamers, and coronal
mass ejections.*

*Interacting loops located
or discounted.*

Line-of-sight effects determined.

3D direction of motion determined.

*Foot points determined by downward
extrapolation.*

*Importance of photospheric features
on heating of coronal loops
established.*

*Nonpotentiality of the magnetic
field determined by comparison
with potential, force-free, and
MHD models.*

*Foot points determined by
downward extrapolation of the
correct magnetic model.*

*Determine the 3D dynamical changes
in the coronal structure.*

*Determine the importance of
flux emergence and reconnection
on CMEs.*

*Assess the importance of
dynamical change and
configuration on coronal
heating.*

*Models for density and
temperature of coronal
loops.*

Stereo | Images

High Cadence
Time Series

Triangulation
Calculate x, y, z

Magnetograms
(B, θ)

Set of Coronal
Loops and Features
in 3D

Build Magnetic Field Models
(Potential, Force-Free, MHD)

Linear
comparison of
observed and calculated
loops and features

Disagree

Modified Magnetic
Boundary Conditions
to Correct Magnetic
Model

Check consistency
of Magnetic Boundary
Conditions

Agree

3D Magnetic Field
Model

Physical Scaling Laws
consistent with
multi-temperature images

Physics Based Rendering
of Loops and Features to
form synthesized Images

Render Surface of
Loops and Features

Reiterate

Resolving cores via
disassembling
the overlapping loops
and using solar rotations

Image
comparison of
Rendered and Observed
Images

Good
Comparisons

Full 3D Coronal Model
based on
Least-Squares Image Analysis

Tomographic Analysis
via
**Multiplicative Algebraic
Reconstruction Techniques**
(MART)

High Cadence
Time Series

Full 3-dimensional Coronal Model
Fully compatible with
Stereographic Images

Physical Characteristics
of Coronal Loops
(Scaling Laws)

Full 3-Dimensional Dynamical Model of the Corona
X, Y, Z, T, n

(consistent with 3D observations)